LETTER

Magnetic Properties and Kondo Effect in Ce_3TiBi_5 under High Pressure

Magnetic Properties and Kondo Effect in Ce_3TiBi_5 under High Pressure

L.C. Fu(傅立承)[1,2], W.J. Cheng(程文静)[1], L.C. Shi(史鲁川)[2,3], B.S. Min(闵保森)[2,3], Y. Peng(彭毅)[2,3], J. Zhang(张俊)[2], J. Song(宋静)[2], Z. Deng(邓正)[2], J.F. Zhao(赵建发)[2], Y. Liu(刘影)[4], J.L. Zhu(朱金龙)[1,4*], J.F. Zhang(张建丰)[5*], X.C. Wang(望贤成)[2,3*], and C.Q. Jin(靳常青)[2,3*]

[1]*Department of Physics, State key laboratory of quantum functional materials, and Guangdong Basic Research Center of Excellence for Quantum Science, Southern University of Science and Technology (SUSTech), Shenzhen 518055, China*
[2]*Beijing National Laboratory for Condensed Matter Physics, Institute of Physics, Chinese Academy of Sciences, Beijing 100190, China*
[3]*School of Physics, University of Chinese Academy of Sciences, Beijing 100190, China*
[4]*Quantum Science Center of Guangdong-Hong Kong-Macao Greater Bay Area (Guangdong), Shenzhen 518045, China*
[5]*Center for High Pressure Science & Technology Advanced Research, Beijing 100193, China*

(Received 14 August 2025; accepted manuscript online 28 November 2025)

The magnetic properties and Kondo effect in Ce_3TiBi_5 with a quasi-one-dimensional structure were investigated using *in situ* high-pressure resistivity measurements up to 48 GPa. At ambient pressure, Ce_3TiBi_5 undergoes an antiferromagnetic (AFM) transition at $T_N \sim 5$ K. Under high pressures within 8.9 GPa, we find that Kondo scattering contributes differently to the high-temperature resistance, $R(T)$, depending on the applied current direction, demonstrating a significantly anisotropic Kondo effect. The complete P–T phase diagram has been constructed, in which the pressure dependence of T_N exhibits a dome-like shape. The AFM order remains robust under pressure, even when the coherence temperature T^* far exceeds 300 K. We attribute the observed anisotropic Kondo effect and the robust AFM to the underlying anisotropy in electronic hybridization under high pressure.

DOI: 10.1088/0256-307X/43/1/010705 CSTR: 32039.14.0256-307X.43.1.010705

1. Introduction. Heavy fermion systems have attracted considerable attention due to their rich physics, which stems from the coupling between conducting electrons and localized f-electrons (c–f coupling), including the Ruderman–Kittel–Kasuya–Yosida (RKKY) interaction and Kondo coupling.[1–5] The RKKY interaction favors the formation of magnetic order, whereas the Kondo coupling screens magnetic moments and leads to a nonmagnetic state. The strengths of both the RKKY and Kondo couplings depend on the c–f coupling strength J_0 and can be tuned by magnetic field or pressure. For small J_0, the RKKY interaction dominates, resulting in a magnetically ordered ground state. As J_0 increases, the Kondo coupling gradually becomes dominant and suppresses the magnetic order. When the magnetic order is fully suppressed, a quantum critical point and heavy fermion superconductivity typically emerge.[6–9] This physical picture is well described by the Doniach phase diagram.[10]

Furthermore, the two-fluid model has been widely adopted to describe the physics of the Kondo lattice.[11–15] In this model, the coherence temperature T^*, which signifies the onset of collective c–f hybridization, is a crucial parameter. Above T^*, all f-electrons are localized and behave as uncoupled magnetic impurities at lattice sites. Below T^*, a portion of the localized f-electrons hybridize with the conduction band, forming itinerant heavy electrons in a so-called "Kondo liquid". The remaining localized f-electrons interact with each other, constituting a "spin liquid". The collective hybridization effectiveness f_0, which reflects the competition between the RKKY and Kondo couplings, ultimately determines the ground state.

Compounds with the Hf_5Sn_3Cu-anti-type structure provide an excellent platform for exploring anisotropic physics due to their quasi-one-dimensional (quasi-1D) character.[16–30] Among them, Ce_3TiBi_5 has been identified and studied as a heavy fermion compound.[29,31,32] As shown in Fig. 1(a), the crystal structure of Ce_3TiBi_5 consists of face-sharing $TiBi_6$ octahedral chains, Bi chains, and zigzag Ce chains running along the c-axis. Ce_3TiBi_5 exhibits an antiferromagnetic (AFM) transition at approximately 5 K with a non-collinear magnetic structure, and its Sommerfeld coefficient is nearly 210 mJ/(Ce·mol·K^2).[29,31–33] The effect of pressure on this AFM transition has been investigated up to 8 GPa.[31] With increasing pressure, the Néel temperature (T_N) first rises to a maximum of 10.2 K at 6 GPa and then decreases at higher pressures. Interestingly, the high-temperature resistivity along the c-axis, $\rho^{\parallel c}$, evolves from metallic behavior to a $-\ln(T)$ dependence under high pressure.[31] Furthermore, at ambient pressure, the in-plane resistivity $\rho^{\perp c}$ at 300 K is six times larger than $\rho^{\parallel c}$, highlighting the strong electrical anisotropy.[29]

High pressure is a powerful tool for manipulating the physical properties of heavy fermion systems.[34–36] In this work, we investigated the magnetic properties of Ce_3TiBi_5

*Corresponding authors. Email: zhujl@sustech.edu.cn; jianfeng.zhang@hpstar.ac.cn; wangxiancheng@iphy.ac.cn; jin@iphy.ac.cn

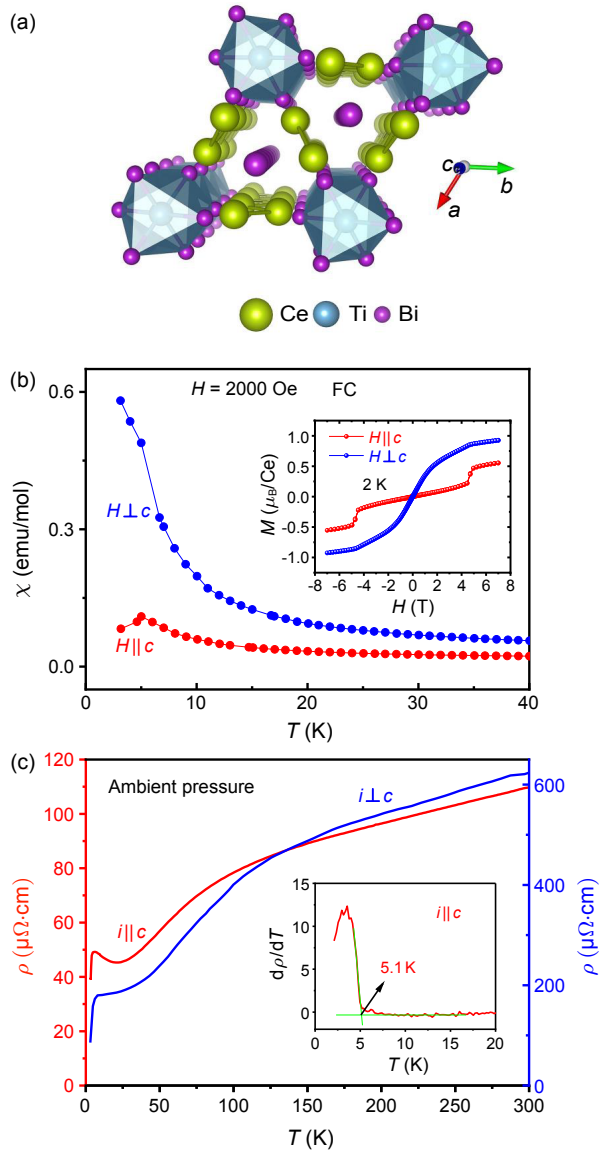

Fig. 1. (a) The sketch of the crystal structure of Ce_3TiBi_5. (b) The temperature dependence of susceptibility of Ce_3TiBi_5 measured in FC conditions under $H = 2000$ Oe with H parallel and perpendicular to the c-axis, respectively. The inset is the isothermal magnetization curve measured at 2 K. (c) The resistivity data at ambient pressure for a single crystal sample Ce_3TiBi_5. The $\rho^{\perp c}$ data are extracted from the reference by G. Motoyama *et al.*[29] The inset is the $d\rho/dT$ curve to determine T_N.

and examined the effect of pressure on its magnetic transition temperature and Kondo effect over an extended pressure range. Furthermore, we measured the resistivity along two different crystallographic directions, revealing an anisotropic Kondo effect in Ce_3TiBi_5. From the high-pressure resistivity data, we extracted the Néel temperature T_N and the coherence temperature T^*, thereby constructing a complete pressure–temperature (P–T) phase diagram. It is proposed that the observed anisotropic Kondo effect and the robust AFM could be attributed to the underlying anisotropy in electronic hybridization under high pressure.

2. Experiments. Single crystals of Ce_3TiBi_5 were grown using the Bi self-flux method. Starting materials included Ce lumps (Alfa, 99.9%), Ti powder (Alfa, 99.99%), and Bi powder (Alfa, 99.99%). These were loaded into an alumina crucible in a molar ratio of Ce:Ti:Bi = 3:1:10, sealed in a quartz tube under vacuum, and heated to 1000 ℃. After holding at this temperature for 10 hours, the assembly was slowly cooled at a rate of 3 ℃/h to 500 ℃. The excess Bi flux was removed using a centrifuge, yielding needle-shaped crystals.

At ambient pressure, electrical resistivity was measured by the standard four-probe method, and DC magnetization was characterized using a Quantum Design Magnetic Property Measurement System (MPMS). For high-pressure resistance measurements, the Van der Pauw four-electrode method was employed with an applied current of 2 mA.[37,38] A needle-shaped crystal was broken into pieces, and a regularly shaped flake (approximately 60 μm in size) was selected for the experiment.

Pressure was applied using a diamond anvil cell fabricated from non-magnetic beryllium-copper alloy, featuring a culet diameter of 300 μm. A T301 stainless steel gasket was pre-indented to a thickness of 30 μm, and a hole of 150 μm in diameter was drilled as the sample chamber. The gasket was electrically insulated from the electrodes by a layer of cubic boron nitride mixed with epoxy. NaCl powder was used as the pressure-transmitting medium. The pressure was calibrated at room temperature by measuring the shift of the R1 fluorescence line of a ruby sphere placed near the sample.[39]

3. Results. Figure 1(b) shows the temperature-dependent magnetic susceptibility, $\chi(T)$, of a Ce_3TiBi_5 single crystal measured in a field-cooling (FC) mode with an external field of $H = 2000$ Oe applied parallel and perpendicular to the c-axis, respectively. For $H \parallel c$, the $\chi(T)$ curve exhibits a sharp peak at 5 K, indicating an AFM transition, consistent with previous reports.[29] For $H \perp c$, the susceptibility is larger and continues to increase below T_N, where only a subtle kink marks the transition. The inset of Fig. 1(b) displays the isothermal magnetization curves measured at 2 K. The magnetization for $H \perp c$ is larger than that for $H \parallel c$, consistent with the $\chi(T)$ data, suggesting that the c-axis is the hard magnetization axis. Additionally, a clear jump occurs at approximately 4.8 T for $H \parallel c$, signaling a metamagnetic transition.

The ambient-pressure resistivity $\rho^{\parallel c}$ is shown in Fig. 1(c), with $\rho^{\perp c}$ data extracted from the report by G. Motoyama *et al.*[29] At room temperature, $\rho^{\parallel c}$ is nearly six times smaller than $\rho^{\perp c}$, demonstrating strong resistivity anisotropy. Both $\rho^{\parallel c}$ and $\rho^{\perp c}$ show a pronounced drop around 100 K and an upturn below approximately 30 K. The drop is attributed to the combined effects of Kondo scattering and the crystalline electric field (CEF), while the low-temperature upturn directly evidences the Kondo effect. The Néel temperature $T_N \approx 5.1$ K, identified from the temperature derivative of resistivity [see inset of Fig. 1(c)] as the onset of a rapid increase in $d\rho/dT$, agrees with the value determined from $\chi(T)$ measurements.

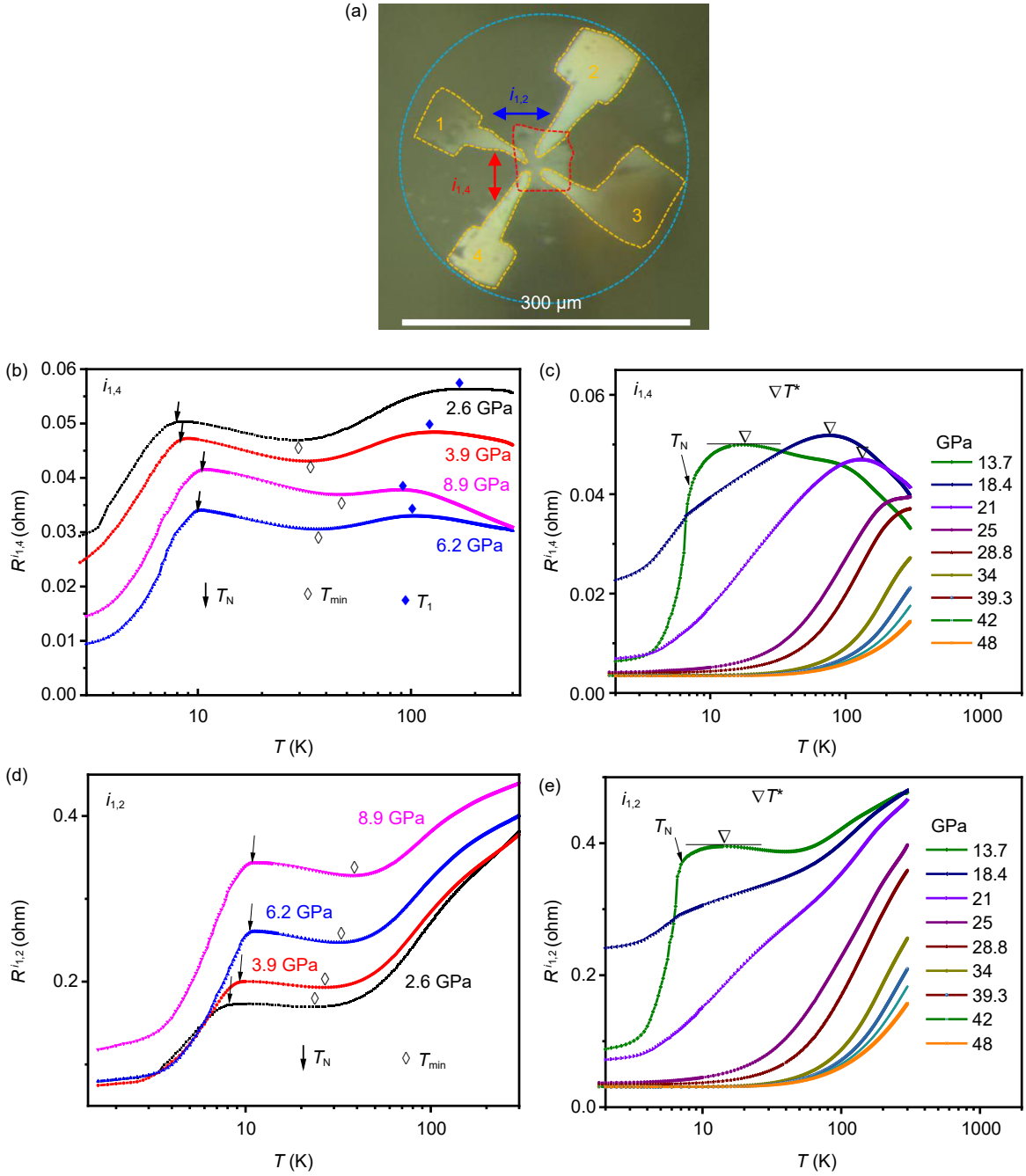

Fig. 2. (a) The image of the high-pressure sample chamber and electrodes arrangement for high-pressure resistance measurement. The blue dashed circle shows the culet of diamond with a diameter of 300 μm, the dashed red square denotes the sample, and the four brown dashed shapes indicate the inner electrodes of Pt. $R^{i_{1,4}}$ was measured with $i_{1,4}$ and $v_{2,3}$ while $R^{i_{1,2}}$ was measured with $i_{1,2}$ and $v_{3,4}$. (b)–(e) Temperature dependence of resistance $R^{i_{1,4}}$ and $R^{i_{1,2}}$ for Ce_3TiBi_5 sample under different pressures plotted on a logarithmic temperature scale. The arrows mark T_N; solid blue diamonds represent T_1 related to CEF excitation energy; hollow diamonds denote T_{min}; and an inverse triangle indicates the coherence temperature T^*.

These ambient-pressure results are in excellent agreement with other recent works[29,32] and confirm the high quality of our single crystals.

To investigate the pressure dependence of the AFM transition and Kondo effect, we performed resistance measurements under high pressure, up to 48 GPa. Figure 2(a) shows the sample chamber configuration, including the electrode arrangement and the sample. Resistances along two different directions have been measured with $i_{1,4}$, $v_{2,3}$ and $i_{1,2}$, $v_{3,4}$, respectively. Figures 2(b)–2(e) display the corresponding high-pressure resistance curves on a logarithmic temperature scale. At 2.6 GPa, the room-temperature resistance $R^{i_{1,4}}$ is 0.055 Ω, nearly seven times smaller than $R^{i_{1,2}}$ (0.38 Ω). This anisotropy under pressure is comparable to the difference between $\rho^{\parallel c}$ and $\rho^{\perp c}$ at ambient pressure, indicating that $R^{i_{1,4}}$ and $R^{i_{1,2}}$ primarily reflect the resistance along ($\rho^{\parallel c}$) and perpendicular ($\rho^{\perp c}$) to the c-axis, respectively.

Figures 2(b) and 2(d) present the temperature-dependent $R^{i_{1,4}}$ and $R^{i_{1,2}}$ under pressures up to 8.9 GPa. $R^{i_{1,4}}$ initially decreases with pressure but increases above 6.2 GPa, whereas $R^{i_{1,2}}$ increases monotonically over the same range. Such a resistance increase under pressure has been reported in other heavy fermion systems [40–42] and is attributed to the enhancement of Kondo scattering. While pressure typically broadens electronic bands and reduces resistivity, in heavy fermion systems it also increases the bandwidth of the local f-orbitals. This pushes the f-band top closer to the Fermi level, thereby enhancing Kondo scattering and leading to an overall increase in resistivity. The non-monotonic variation of $R^{i_{1,4}}$ in Fig. 2(b) reflects a competition between conventional band broadening and Kondo scattering.

At high temperatures, $R^{i_{1,4}}$ exhibits metallic behavior at ambient pressure but develops a logarithmic increase upon cooling under high pressures, as previously reported. [31] This suggests that Kondo scattering dominates $R^{i_{1,4}}$ under these conditions. A resistance maximum is observed in the $R^{i_{1,4}}$ curves [marked by solid blue diamonds in Fig. 2(b)] at a temperature T_1, which decreases with increasing pressure. Below T_1, the resistance decrease results from the interplay between the Kondo effect and the CEF. As the temperature drops below the energy of higher-lying CEF levels, electrons redistribute into lower-lying states, reducing the Kondo scattering rate. In contrast, $R^{i_{1,2}}$ retains its metallic behavior at high temperatures under pressure, indicating a negligible contribution from Kondo scattering, with the Kondo–CEF interplay only manifesting as a weak hump. The distinct responses of $R^{i_{1,4}}$ and $R^{i_{1,2}}$ demonstrate an anisotropic Kondo effect in Ce_3TiBi_5. At low temperatures, both $R^{i_{1,4}}$ and $R^{i_{1,2}}$ exhibit a logarithmic upturn due to the Kondo effect, leading to a resistance minimum (marked by hollow diamonds) at a temperature $T_{\rm min}$. The increase of $T_{\rm min}$ with pressure further confirms the enhancement of Kondo scattering under pressure. Below this upturn, a sharp drop in resistance marked by arrows signifies the onset of AFM ordering.

Figures 2(c) and 2(e) present the temperature dependence of $R^{i_{1,4}}$ and $R^{i_{1,2}}$ under pressures above 8.9 GPa. At 13.7 GPa, the low-temperature logarithmic upturns in both $R^{i_{1,4}}$ and $R^{i_{1,2}}$ are followed by a broad resistance maximum at a temperature denoted as T^* (marked by inverted hollow triangles). As clearly seen in Fig. 2(c), T^* for $R^{i_{1,4}}$ shifts progressively to higher temperatures with pressure, exceeding 300 K above 34 GPa. The rapid decrease of $R^{i_{1,4}}$ below T^* indicates the onset of coherent Kondo scattering. In contrast, T^* cannot be determined from the $R^{i_{1,2}}$ due to its persistently metallic behavior at high pressures [see Fig. 2(e)].

From Figs. 2(b)–2(e), we extracted the resistance at a fixed temperature of 250 K as a function of pressure for both $R^{i_{1,4}}$ and $R^{i_{1,2}}$, as shown in Fig. S1 of the Supplementary Materials (SM). The resistance increases smoothly above 6.2 GPa, reaches a maximum around 18–21 GPa, and then decreases at higher pressures. The initial increase is attributed to the enhancement of Kondo scattering, while the subsequent decrease signifies that coherent Kondo scattering begins to dominate charge transport. No anomalous resistance change indicative of a structural transition is observed in the $R(P)$ curves, suggesting that the crystal structure remains stable over the entire experimental pressure range.

To investigate the pressure effect on the AFM transition, we determined the Néel temperature $T_{\rm N}$ at various pressures from the temperature derivative of $R^{i_{1,4}}$, as shown in Figs. 3(a)–3(l). $T_{\rm N}$ initially increases with pressure, reaches a maximum of 10.9 K at 8.9 GPa, and then gradually decreases to 3.4 K at 39.3 GPa. Above 42 GPa, $T_{\rm N}$ drops below 2 K. The dR/dT data with current $i_{1,2}$ are presented in Figs. S2(a)—S2(l), from which the extracted $T_{\rm N}$ values exhibit a similar pressure dependence. A notable change in the resistance behavior occurs around 21 GPa. In the pressure range of 13.7–21 GPa, coherent Kondo scattering begins to develop at a relatively low T^*, leading to coexistence between incoherent and coherent Kondo scattering. This results in a negative curvature in $R(T)$, which obscures the signature of the magnetic transition in the resistivity, particularly at 21 GPa. When the pressure exceeds 21 GPa, coherent Kondo scattering is fully established at a much higher T^* and dominates the transport. Consequently, the AFM transition becomes clearly visible again as a kink in the resistance curves [see Figs. 3(h)–3(k)], at a temperature consistent with that identified from the derivative peaks. The establishment of coherent Kondo scattering with high T^* also causes a significant reduction in resistance; e.g., $R(15\,{\rm K})$ drops from $\sim 0.04\,\Omega$ at 8.9 GPa to $\sim 0.0035\,\Omega$ at 39 GPa. Concurrently, $T_{\rm N}$ is suppressed from $\sim$7–11 K to $\sim$3–5 K. This explains why the resistance drop at the magnetic transition above 21 GPa is much smaller than that at lower pressures. Therefore, it is suggested that the AFM phase likely persists beyond 21 GPa. Nevertheless, we cannot rule out other origins for the resistance kinks at high pressures ($P > 28.8$ GPa), such as residual magnetism due to pressure inhomogeneity, which deserves further investigation.

Figures 4(a) and 4(b) present fits to the low-temperature $R^{i_{1,4}}$ data using the power-law form $R = R_0 + AT^n$, where R_0 is the residual resistance, A is the coefficient, and n is the exponent. Since coherent Kondo scattering begins to emerge at low temperatures in the pressure range of 13.7–21 GPa and may complicate the analysis, only data above 21 GPa were included in the fitting. The extracted exponent n increases gradually from 1.5 to 3.23 as pressure rises from 25 GPa to a maximum of 48 GPa. For the data at 18.4 and 21 GPa, the negative curvature in $R^{i_{1,4}}(T)$ suggests an exponent $n < 1$ as seen in Figs. S3(a)–S3(c) of the SM, likely arising from the interplay between incoherent and coherent Kondo scattering. Above 21 GPa, where coherent Kondo scattering starts to dominate the transport, the exponent n increases systematically. Therefore, the values of $n \approx 1.5$–1.59 at 25–28.8 GPa cannot be taken as evidence for non-Fermi-liquid behavior. As the AFM transition is suppressed toward zero temperature, the expected quantum criticality with $n \sim 1$ has not been observed above 5 K.

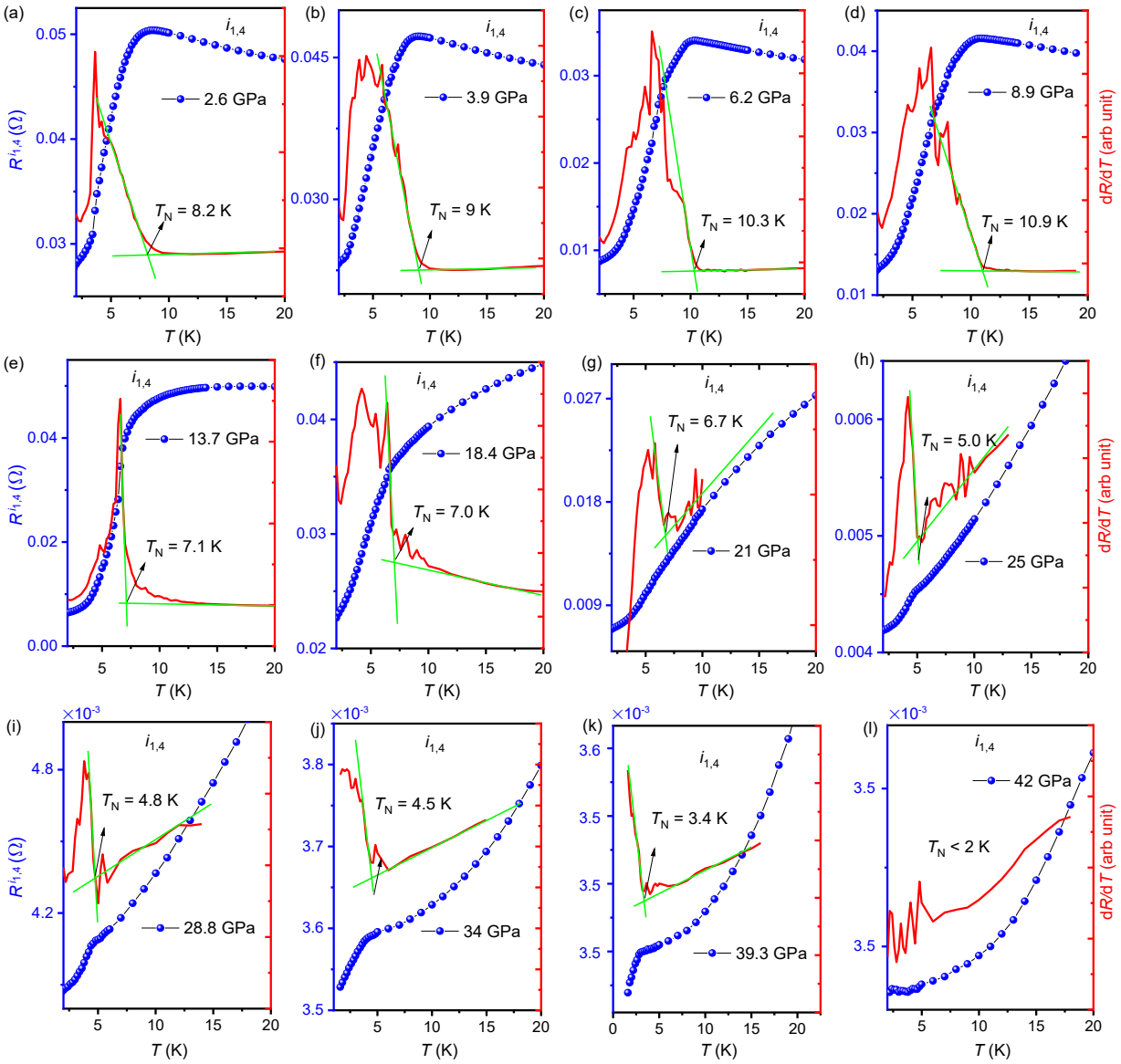

Fig. 3. The resistance data of $R^{i_{1,4}}$ and their temperature derivative under different pressures, from which the T_N values can be clearly determined.

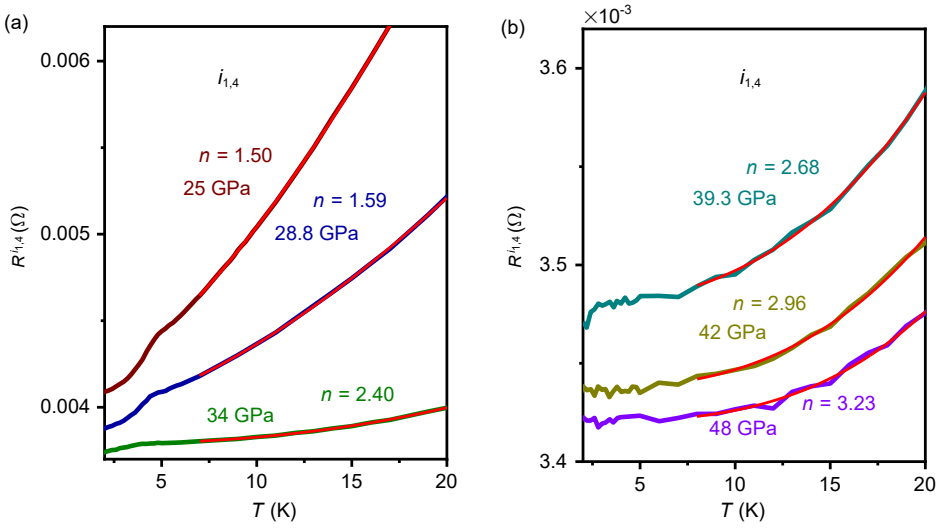

Fig. 4. The resistance of $R^{i_{1,4}}$ for the Ce_3TiBi_5 sample under different pressures in the low-temperature region. The red lines are the fittings using the formula $R = R_0 + AT^n$.

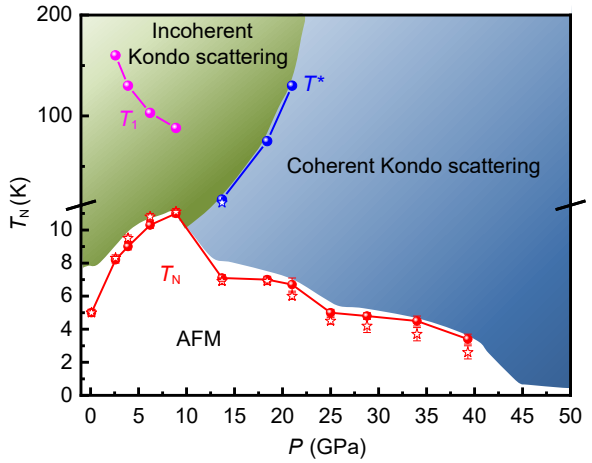

Fig. 5. The P–T phase diagram of Ce_3TiBi_5, showing the pressure dependence of T_N, T^*, and T_1. The red, blue, and purple solid circles denote T_N, T^*, and T_1 determined from $R^{i_{1,4}}$ data, respectively. The red and blue hollow stars denote T_N and T^* determined from $R^{i_{1,2}}$ data, respectively.

This suggests that fitting to data at much lower temperatures would be required to detect non-Fermi-liquid behavior. A similar evolution of n with pressure is observed in the fits to $R^{i_{1,2}}(T)$, as shown in Figs. S4(a) and S4(b) of the SM.

Based on the values of T_N, T^*, and T_1 extracted from both $R^{i_{1,4}}(T)$ and $R^{i_{1,2}}(T)$, we construct the pressure-temperature phase diagram shown in Fig. 5. The Néel temperature T_N exhibits a dome-shaped dependence on pressure, reaching a maximum at 8.9 GPa and eventually being suppressed below 2 K above 42 GPa. This dome-like behavior reflects the competition between the Kondo effect and the RKKY interaction. The temperature T_1, associated with CEF splitting, decreases with increasing pressure. This decrease results from the competition between two opposing effects of pressure: the compression of coordination polyhedron, which tends to increase CEF splitting, and the broadening of electronic bandwidth, which reduces the energy gap between CEF levels. Meanwhile, Kondo coherence emerges at $T^* \sim 17$ K for 13.7 GPa and rises rapidly with further compression, exceeding 300 K near the critical pressure of 45 GPa.

4. Discussion. An anisotropic Kondo effect is observed in Ce_3TiBi_5 under high pressure, where the high-temperature resistances $R^{i_{1,4}}$ and $R^{i_{1,2}}$ are dominated by Kondo scattering and electron–phonon scattering, respectively. A similar anisotropic Kondo effect has been reported in the Kondo semiconductor $CeFe_2Al_{10}$, which exhibits an anisotropic electronic structure and c–f hybridization.[43–45] To understand this anisotropic Kondo effect in Ce_3TiBi_5, we perform the first-principles calculation[46] of its electronic structure, the details of which are provided in the SM. Figures 6(a) and 6(b) present the paramagnetic band structures, where the circle sizes indicate the projecting weights of Ce sd (green), Ti sd (orange), and Bi sp (purple) orbitals. Here, a salient feature is the quasi-1D band spectra derived from Bi atomic orbitals (purple circles). To examine the hybridization between the localized Ce 4f moments and the conduction electrons near the Fermi level, we included the Ce 4f states in pseudopotential calculations. For illustration, we adopted a ferromagnetic configuration. In Figs. 6(c) and 6(d), red and blue denote majority (spin-up) and minority (spin-down) channels, respectively, and dot sizes represent the Ce 4f orbital weight. Near the Fermi level, the Ce 4f states primarily hybridize with Bi p orbitals on the quasi-1D bands along the Γ–A direction, demonstrating anisotropic c–f hybridization. Notably, within these quasi-1D states, the Ce 4f weight is markedly increased at 10 GPa, indicating strongly enhanced c–f hybridization under pressure, which can also be seen in Fig. S5 of the SM for the corresponding Fermi-surface distributions. This enhancement is further corroborated by crystal orbital Hamilton population (COHP) analysis[47] in Figs. S6(e) and S6(f). At 10 GPa, around the Fermi energy, the hybridization between Ce 4f orbital and other atomic orbitals is substantially stronger than that at ambient pressure in both majority (antibonding) and minority (bonding) spin channels. Collectively, these results suggest that the anisotropic Kondo effect in Ce_3TiBi_5 likely originates from pressure-enhanced anisotropic c–f hybridization.

Furthermore, $CeCo_2Ga_8$, with its pronounced quasi-1D Ce-chain structure, shows strong anisotropy in Kondo coherence formation: coherence develops at 17 K along the c-axis, while incoherent scattering persists down to 2 K within the ab-plane.[48,49] It has been proposed that the coherence temperature is governed not only by the Kondo energy scale but also by the lattice properties of ions carrying local f-electrons.[49] In contrast, compressed Ce_3TiBi_5 shows a much weaker anisotropy in Kondo coherence. At 13.7 GPa, the coherence temperature T^* is about 17 K for $R^{i_{1,4}}$ and 14 K for $R^{i_{1,2}}$, as shown in Figs. 2(c) and 2(e). This modest anisotropy can be understood structurally: although Ce_3TiBi_5 possesses a strong quasi-1D character, the intra-chain Ce-Ce distance (3.9398 Å) is only slightly shorter than the inter-chain distance (4.8835 Å). Therefore, the reduced anisotropy of Kondo coherence in Ce_3TiBi_5 can be attributed to its less one-dimensional Ce lattice.

Besides the anisotropic Kondo effect, another intriguing observation in Ce_3TiBi_5 is the robustness of the AFM order under pressure, despite the establishment of Kondo coherence with a very high characteristic temperature T^*. This indicates that local moments from f-electrons still persist even under well-developed Kondo screening. According to the two-fluid model,[11] the ground state is governed by the collective hybridization effectiveness f_0 between f- and conduction electrons. When $f_0 < 1$, the local spin liquid dominates, yielding a magnetic ground state via the RKKY interaction. As f_0 approaches 1, the magnetic transition temperature is suppressed to zero. The persistence of AFM order thus implies that pressure only inefficiently enhances the collective hybridization effectiveness. Electronic structure calculations reveal that a primary effect of pressure is to enhance hybridization predominantly along the c-axis. Therefore, we propose that the limited

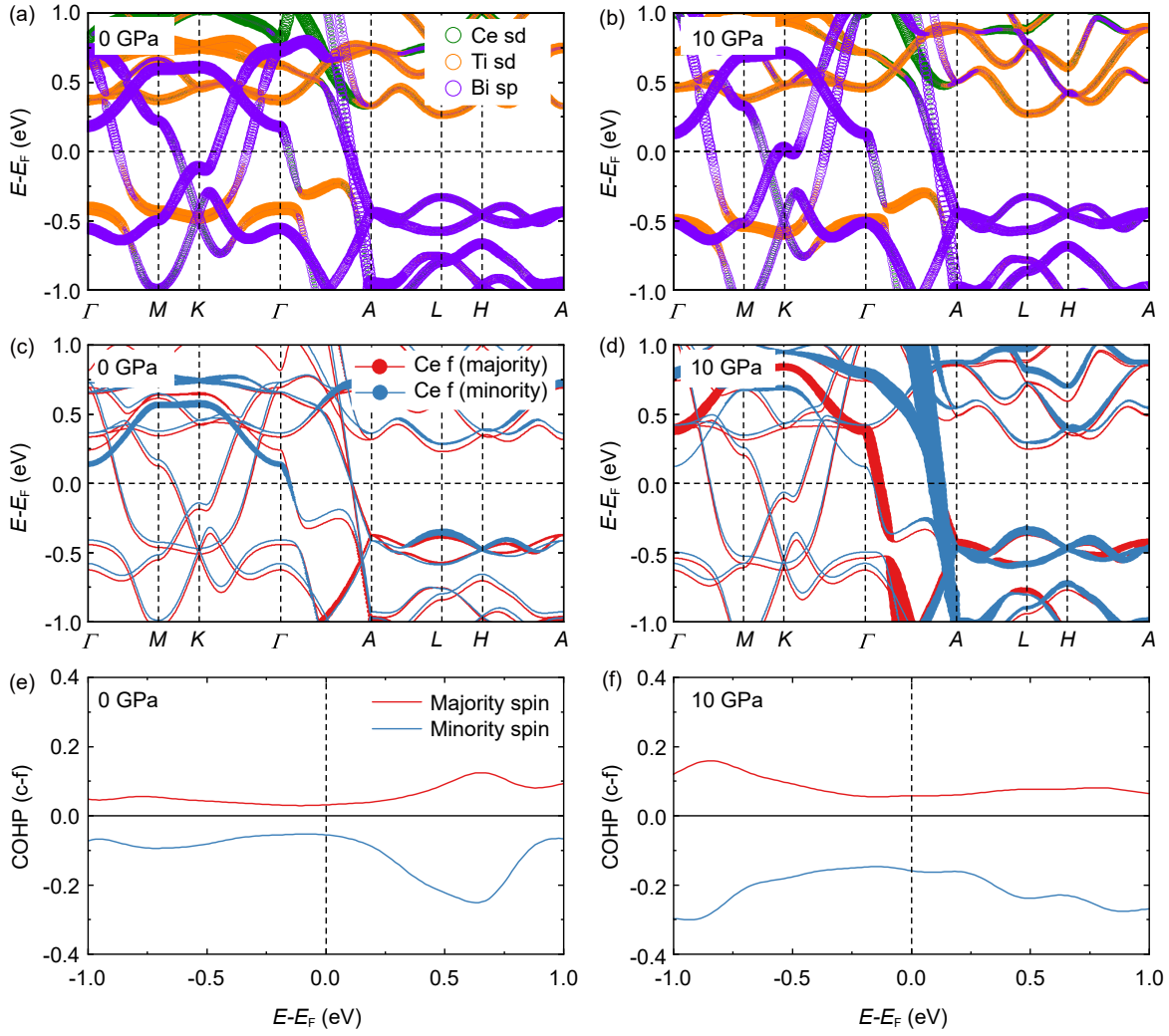

Fig. 6. The calculated paramagnetic band structure of Ce_3TiBi_5 at (a) ambient pressure and (b) 10 GPa. The circle sizes represent the projecting weights of Ce sd (green), Ti sd (orange), and Bi sp (purple) orbitals. The calculated spin-polarized band structure at (c) ambient pressure and (d) 10 GPa. Red and blue denote majority (spin-up) and minority (spin-down) channels, respectively, and dot sizes represent the Ce 4f orbital weight. The COHP distribution between the Ce 4f orbital and other atomic orbitals at (e) ambient pressure and (f) 10 GPa.

enhancement of collective hybridization is related to strongly anisotropic hybridization in this system under high pressure.

5. Conclusion. We have investigated the magnetic properties and Kondo effect of the quasi-1D heavy fermion compound Ce_3TiBi_5 under high pressure. Pressure enhances Kondo scattering, leading to an increase in both $R^{i_{1,4}}$ and $R^{i_{1,2}}$. A significantly anisotropic Kondo effect is observed under high pressure, which is attributed to pressure-enhanced anisotropic hybridization between f and conduction electrons. From the extracted AFM transition temperature T_N and coherence temperature T^*, we constructed a pressure-temperature phase diagram. The dome-shaped dependence of T_N on pressure reflects the competition between the Kondo effect and the RKKY interaction. The AFM order is completely suppressed near 45 GPa, where the coherence temperature T^* far exceeds 300 K. The limited enhancement of collective hybridization with pressure is likely related to the underlying anisotropy in electronic hybridization under high pressure.

Acknowledgements. This work was supported by the National Key Research and Development Program of China, the National Natural Science Foundation of China (Grant Nos. 2024YFA1408000, 12474097, and 2023YFA1406001), the Guangdong Provincial Quantum Science Strategic Initiative (Grant No. GDZX2201001), the Center for Computational Science and Engineering at Southern University of Science and Technology, the Major Science and Technology Infrastructure Project of Material Genome Big-science Facilities Platform supported by Municipal Development and Reform Commission of Shenzhen (for J.L.Z. and Y.L.), and the Chinese funding sources applied via HPSTAR. Some experiments are supported by the Synergic Extreme Condition User Facility.

References

[1] Stewart G R 1984 *Rev. Mod. Phys.* **56** 755

[2] Mathur N D, Grosche F M, Julian S R, Walker I R, Freye D M, Haselwimmer R K W, and Lonzarich G G 1998 *Nature* **394** 39

[3] Gegenwart P, Si Q, and Steglich F 2008 *Nat. Phys.* **4** 186

[4] Chen Q Y, Xu D F, Niu X H, Jiang J, Peng R, Xu H C, Wen C H P, Ding Z F, Huang K, Shu L, Zhang Y J, Lee H, Strocov V N, Shi M, Bisti F, Schmitt T, Huang Y B, Dudin P, Lai X C, Kirchner S, Yuan H Q, and Feng D L 2017 *Phys. Rev. B* **96** 045107

[5] Wirth S and Steglich F 2016 *Nat. Rev. Mater.* **1** 16051

[6] Steglich F, Aarts J, Bredl C D, Lieke W, Meschede D, Franz W, and Schafer H 1979 *Phys. Rev. Lett.* **43** 1892

[7] Shen B, Zhang Y, Komijani Y, Nicklas M, Borth R, Wang A, Chen Y, Nie Z, Li R, Lu X, Lee H, Smidman M, Steglich F, Coleman P, and Yuan H Q 2020 *Nature* **579** 51

[8] Movshovich R, Graf T, Mandrus D, Thompson J D, Smith J L, and Fisk Z 1996 *Phys. Rev. B* **53** 8241

[9] Hegger H, Petrovic C, Moshopoulou E G, Hundley M F, Sarrao J L, Fisk Z, and Thompson J D 2000 *Phys. Rev. Lett.* **84** 4986

[10] Doniach S 1977 *Physica B & C* **91** 231

[11] Nakatsuji S, Pines D, and Fisk Z 2004 *Phys. Rev. Lett.* **92** 016401

[12] Yang Y F, Fisk Z, Lee H O, Thompson J D, and Pines D 2008 *Nature* **454** 611

[13] Yang Y F and Pines D 2008 *Phys. Rev. Lett.* **100** 096404

[14] Yang Y F 2016 *Rep. Prog. Phys.* **79** 074501

[15] Ji X Y, Luo X B, Chen Q Y, Feng W, Hao Q Q, Liu Q, Zhang Y, Liu Y, Wang X Y, Tan S Y, and Lai X C 2022 *Phys. Rev. B* **106** 125120

[16] Zhang J, Jia Y T, Wang X C, Li Z, Duan L, Li W M, Zhao J F, Cao L P, Dai G Y, Deng Z, Zhang S J, Feng S M, Yu R Z, Liu Q Q, Hu J P, Zhu J L, and Jin C Q 2019 *NPG Asia Materials* **11** 60

[17] Zhang J, Duan L, Wang Z, Wang X C, Zhao J F, Jin M L, Li W M, Zhang C L, Cao L P, Deng Z, Hu Z W, Agrestini S, Valvidares M, Lin H J, Chen C T, Zhu J L, and Jin C Q 2020 *Inorg. Chem.* **59** 5377

[18] Zhang J, Komarek A C, Jin M, Wang X C, Jia Y T, Zhao J F, Li W M, Hu Z W, Peng W, Wang X, Tjeng L H, Deng Z, Yu R Z, Feng S M, Zhang S J, Liu M, Yang Y F, Lin H J, Chen C T, Li X D, Zhu J L, and Jin C Q 2021 *Phys. Rev. Mater.* **5** 054606

[19] Zhang J, Wang X C, Zhou L, Liu G X, Adroja D T, da Silva I, Demmel F, Khalyavin D, Sannigrahi J, Nair H S, Duan L, Zhao J F, Deng Z, Yu R Z, Shen X, Yu R C, Zhao H, Zhao J M, Long Y W, Hu Z W, Lin H J, Chan T S, Chen C T, Wu W, and Jin C Q 2022 *Adv. Mater.* **34** 2106728

[20] Zhang J, Zhang X Y, Xia Y H, Zhao J F, Duan L, Wang G D, Min B S, Cao H B, Dela Cruz C R, Zhao K, Sun H Y, Zhu J L, Zhang J F, Xiang T, Wang X C, and Jin C Q 2023 *Phys. Rev. B* **108** 174423

[21] Duan L, Wang X C, Zhan F Y, Zhang J, Hu Z W, Zhao J F, Li W M, Cao L P, Deng Z, Yu R Z, Lin H J, Chen C T, Wang R, and Jin C Q 2020 *Sci. China Mater.* **63** 1750

[22] Duan L, Zhang J, Wang X C, Zhao J F, Cao L P, Li W M, Deng Z, Yu R Z, Li Z, and Jin C Q 2020 *J. Alloy. Compd.* **831** 154697

[23] Duan L, Wang X C, Zhang J, Hu Z, Zhao J F, Feng Y G, Zhang H L, Lin H J, Chen C T, Wu W, Li Z, Wang R, Zhang J F, Xiang T, and Jin C Q 2022 *Phys. Rev. B* **106** 184405

[24] Zhang C W, Wang Y X, Zheng J X, Du L, Li Y, Han X, Liu E K, Wu Q S, and Shi Y G 2024 *Phys. Rev. Mater.* **8** 034402

[25] Moore S H D, Deakin L, Ferguson M J, and Mar A 2002 *Chem. Mater.* **14** 4867

[26] Matin M, Kulkarni R, Thamizhavel A, Dhar S K, Provino A, and Manfrinetti P 2017 *J. Phys. Condens. Mat.* **29** 145601

[27] Ritter C, Pathak A K, Filippone R, Provino A, Dhar S K, and Manfrinetti P 2021 *J. Phys.: Condens. Matter* **33** 245801

[28] Fu L C, Shi L C, Chen X M, Duan L, Peng Y, Zhang J, Song J, Deng Z, Zhang S J, Zhao J F, Liu Y, Zhang J F, Zhu J L, Wang X C, and Jin C Q 2025 *J. Phys. Condens. Mat.* **37** 015803

[29] Motoyama G, Sezaki M, Gouchi J, Miyoshi K, Nishigori S, Mutou T, Fujiwara K, and Uwatoko Y 2018 *Physica B* **536** 142

[30] Xu Z C, Wang Y X, Zhang C W, Liu H X, Han X, Wu L S, Zhang X M, Wu Q S, and Shi Y G 2024 *Phys. Rev. B* **110** 165106

[31] Tsubouchi M, Motoyama G, Gouchi J, Miyoshi K, Nishigori S, Fujiwara K, Mutou T, and Uwatoko Y 2020 *JPS Conf. Proc.* **30** 011102

[32] Motoyama G, Shinozaki M, Nishigori S, Yamaguchi A, Aso N, Mutou T, Manago M, Fujiwara K, Sumiyama A, and Uwatoko Y 2023 *JPS Conf. Proc.* **38** 011084

[33] Gauthier N, Sibille R, Pomjakushin V, Fjellvag Ø S, Fraser J, Desmarais M, Bianchi A D, and Quilliam J A 2024 *Phys. Rev. B* **109** L140405

[34] Chen Y, Weng Z F, Michael S, Lu X, and Yuan H Q 2016 *Chin. Phys. B* **25** 077401

[35] Huang Y E, Wu F, Wang A, Chen Y, Jiao L, Smidman M, and Yuan H Q 2022 *Chin. Phys. Lett.* **39** 097101

[36] Zhang L B, Dong Q X, Bai J L, Liu Q Y, Cheng J W, Li C D, Liu P Y, Sun Y R, Huang Y, Ren Z A, and Chen G F 2024 *Chin. Phys. B* **33** 067101

[37] Li Z W, He X, Zhang C L, Wang X C, Zhang S J, Jia Y T, Feng S M, Lu K, Zhao J F, Zhang J, Min B S, Long Y W, Yu R C, Wang L H, Ye M Y, Zhang Z S, Prakapenka V, Chariton S, Ginsberg P A, Bass J, Yuan S H, Liu H Z, and Jin C Q 2022 *Nat. Commun.* **13** 2863

[38] Zhang C L, He X, Liu C, Li Z W, Lu K, Zhang S J, Feng S M, Wang X C, Peng Y, Long Y W, Yu R C, Wang L H, Prakapenka V, Chariton S, Li Q, Liu H Z, Chen C F, and Jin C Q 2022 *Nat. Commun.* **13** 5411

[39] Fu L C, Cheng W J, Liu Y, Shi L C, Peng Y, Zhang J, Li Z W, Li X D, Zhu J L, Wang X C, and Jin C Q 2024 *High Press. Res.* **44** 95

[40] Hayashi Y, Takai S, Matsumura T, Tanida H, Sera M, Matsubayashi K, Uwatoko Y, and Ochiai A 2016 *J. Phys. Soc. Jpn.* **85** 034704

[41] Nishioka T, Kawamura Y, Takesaka T, Kobayashi R, Kato H, Matsumura M, Kodama K, Matsubayashi K, and Uwatoko Y 2009 *J. Phys. Soc. Jpn.* **78** 123705

[42] Muramatsu T, Tateiwa N, Kobayashi T C, Shimizu K, Amaya K, Aoki D, Shishido H, Haga Y, and Onuki Y 2001 *J. Phys. Soc. Jpn.* **70** 3362

[43] Kimura S I, Muro Y, and Takabatake T 2011 *J. Phys. Soc. Jpn.* **80** 033702

[44] Muro Y, Yutani K, Kajino J, Onimaru T, and Takabatake T 2013 *J. Korean Phys. Soc.* **63** 508

[45] Tanida H, Nakamura M, Sera M, Kondo A, Kindo K, Nishioka T, and Matsumura M 2014 *J. Phys. Soc. Jpn.* **83** 084708

[46] Blochl P E 1994 *Phys. Rev. B* **50** 17953

[47] Deringer V L, Tchougréeff A L, and Dronskowski R 2011 *J. Phys. Chem. A* **115** 5461

[48] Cheng K, Wang L, Xu Y, Yang F, Zhu H, Ke J, Lu X, Xia Z, Wang J, Shi Y, Yang Y, and Luo Y 2019 *Phys. Rev. Mater.* **3** 021402

[49] Zheng P, Wang C, Xu Y, Wang L, Wu W, Shi Y G, Yang Y F, and Luo J L 2022 *Phys. Rev. B* **105** 035112